Relaxation of a fluid-filled blister on a porous substrate

Danielle L. Chase, Ching-Yao Lai, and Howard A. Stone

Phys. Rev. Fluids **6**, 084101 — Published 18 August 2021

DOI: 10.1103/PhysRevFluids.6.084101

Relaxation of a fluid-filled blister on a porous substrate

Danielle L. Chase,[1] Ching-Yao Lai,[2] and Howard A. Stone[1, *]

[1]*Department of Mechanical and Aerospace Engineering, Princeton University, Princeton, New Jersey 08544, USA.*

[2]*Department of Geosciences, Princeton University, Princeton, New Jersey 08544, USA.*

The relaxation dynamics of a fluid-filled blister between an elastic sheet and a porous substrate are controlled by the deformation of the elastic sheet, the viscous stresses in the pores, and the capillary pressure at the liquid-air interface due to imbibition. We develop a mathematical model to study the effects of varying the permeability of the porous substrate, the bending stiffness of the elastic sheet, and the blister size on the relaxation dynamics. Experiments are conducted by injecting a finite volume of viscous fluid between the porous substrate and an elastic sheet, where fluid first invades the pores, and subsequently, as the pressure in the fluid increases, the elastic sheet is peeled and uplifted from the substrate to form a fluid-filled blister. After injection is stopped, the fracture front is static, and the elastic stresses in the overlying sheet and the capillary pressure at the liquid-air interface drive the drainage of the blister into the pores. We identify two regimes of drainage. For thick sheets and more permeable substrates, drainage is primarily due to the stresses in the deformed elastic sheet, and for thin sheets and less permeable substrates, drainage is driven by the imbibition of the liquid into the pore space. Our model and experiments are relevant to the drainage of fluid-driven fractures in porous media.

I. INTRODUCTION

Fluid-driven fracture involves the injection of a viscous fluid into an elastic material in order to form a fluid-filled cavity. This process is ubiquitous in geophysical systems, including hydraulic fracturing for the extraction of oil and gas [1] and for the creation of enhanced geothermal systems [2], ice sheet uplift due to supraglacial lake drainage [3], and transport of magma in the lithosphere [4]. The interplay of viscous flow and deformation of an elastic material is also relevant in biofluid mechanics involving flow through elastic tubes [5], fractures in epithelial cell sheets [6], subcutaneous injections [7], and soft actuators for robotics [8].

Theoretical elastohydrodynamic models and laboratory experiments have been used to study fluid-driven fracture of elastic media. Such models predict the fracturing dynamics and crack geometry by coupling viscous flow, deformation of the elastic media, and the fracture or delamination energy required to form the crack. One typical laboratory experiment is conducted by injecting viscous fluid into a block of elastic material, like gelatin, to form a penny-shaped cavity [9–11]. In a second type of experiment, fluid is injected between a rigid substrate and an overlying thin elastic sheet, either adhered to the substrate or separated by a thin layer of fluid, to form a fluid-filled blister where viscous flow in the blister is driven by gradients in elastic stresses or hydrostatic pressure [12–14]. Two cases have been proposed to regularize the tip dynamics as the fluid is driven into a narrowing gap. For an adhered sheet, the diverging viscous stresses at the front lead to a vapor tip with the liquid front lagging the fracture front [13, 15]. Alternatively, a prewetting thin fluid film between the substrate and overlying elastic sheet can be used to regularize the tip dynamics by matching the tip region to the interior [12, 16].

A fluid-filled crack formed in porous media, as is common in natural systems, can simultaneously drain into the surrounding media during injection. The dynamics of the formation of a fluid-filled cavity between a porous or permeable substrate and an overlying elastic sheet has been studied theoretically [17, 18]. Another instance of fluid-driven fracturing in porous media is "leak-off", which is a phenomenon in hydraulic fracturing, where, during the fracturing process, some of the high pressure fluid within the crack leaks into the surrounding rock from the crack faces [19]. Following the formation of a fracture, if the injection pressure is removed, the process reverses, and the crack can drain from the site of injection [20]. The drainage of fluid-filled cracks is relevant to many environmental phenomena including flowback in hydraulic fracturing when the injected fluid returns to the surface as wastewater. In porous media, the crack can also drain into the surrounding media after the it has been formed. One example is when, subsequent to the formation of a fluid-filled blister beneath an ice sheet at the ice-bed interface due to supraglacial lake drainage, the elastic stresses in the uplifted ice sheet drive the relaxation of the blister through the subglacial drainage system [21]. To the best of our knowledge, there have been no experimental studies of the drainage of fluid-filled cracks into a surrounding porous media. This topic is the subject of the present paper.

* To whom correspondence should be addressed: hastone@princeton.edu

In particular, we study the relaxation dynamics of a fluid-filled blister between an elastic sheet and a porous substrate driven by bending and stretching of the elastic sheet and the capillary pressure at the liquid-air interface and resisted by the viscous stresses in the pores . We first present a model for relaxation driven by elastic deformation and imbibition in Section II, explain our experimental setup in Section III, and finally, in Section IV, we compare the results of the experiments with our model.

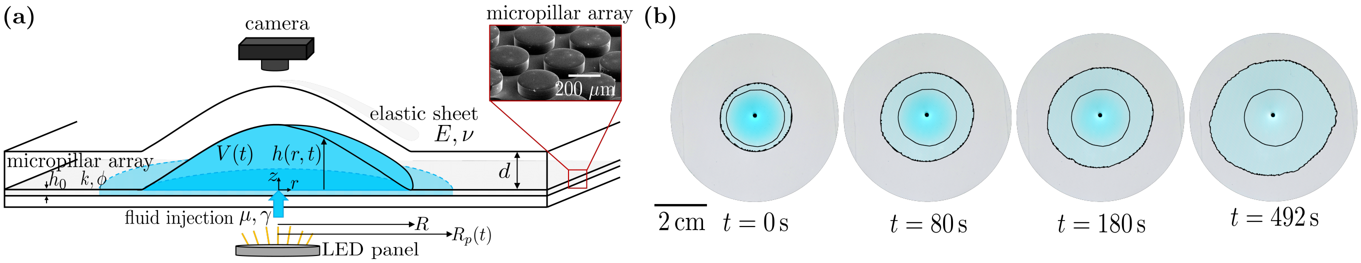

FIG. 1. Blister relaxation experiment. (a) Schematic of experimental setup and theoretical model. (b) Time sequence images of the experimental relaxation dynamics where fluid from the blister (dark blue) drains into the porous substrate (light blue). The blister and fluid front in the pores are outlined.

II. THEORETICAL MODEL

We study the drainage into a porous substrate of a liquid with viscosity μ and surface tension γ from a blister beneath an elastic sheet (Fig. 1). The elastic sheet has thickness d and bending modulus $D = Ed^3/12(1-\nu^2)$, where E is the elastic modulus and ν is Poisson's ratio. The porous substrate has pillars of height h_0, porosity ϕ, and a permeability k. The relaxation is driven by the pressure due to deformation of the elastic sheet and the capillary pressure at the liquid-air interface in the porous substrate due to imbibition and is resisted by the viscous stresses due to the flow through the porous substrate. To form the blister, a fixed volume of fluid V_{tot} is injected between the porous substrate and the elastic sheet, where the pore space is initially filled with air. The blister has initial volume V_0 and radius R, and our experimental observations confirm that the radius of the blister is constant throughout the time of the relaxation experiment (as shown in Fig. 3c). The blister radius and initial volume are determined by parameters including: bending modulus of the elastic sheet, adhesion between the porous substrate and overlying elastic sheet, fluid injection rate, fluid viscosity, and wettability and permeability of the substrate. The process of the blister formation is the subject of future work.

We assume axisymmetry for both the blister shape and the drainage into the pores. The blister volume is given by $V(t)$ and the fluid volume in the pores is $\phi h_0 \pi R_p(t)^2$, where $R_p(t)$ is the extent of the invasion of fluid into the porous substrate. The total volume in the system is thus

$$V_{tot} = V(t) + \phi h_0 \pi R_p(t)^2. \tag{1}$$

The volume flux out of the blister is defined by the time derivative of Eq. (1).

By mass conservation, the horizontal flux in the pores outside the blister must be constant along r, $\frac{\partial(r\phi u_p)}{\partial r} = 0$, where u_p is the depth-averaged velocity of the fluid in the pores. Therefore, $r\phi u_p|_r = R_p \phi u_p|_{R_p}$. At the fluid-air boundary, $r = R_p(t)$, and the velocity in the pores is defined as $u_p|_{r=R_p} = \frac{dR_p}{dt}$. The volume flux from the blister is then defined in terms of the fluid velocity.

$$\frac{dV}{dt} = -2\pi\phi h_0 r u_p. \tag{2}$$

A. Flow in the porous substrate

The fluid flow in the porous substrate follows Darcy's law, $\frac{\partial p}{\partial r} = -\frac{\phi\mu}{k} u_p$. Using Eq. (2), Darcy's law can be written in terms of the volume flux from the blister and integrated from the radial boundary of the blister, $r = R$, to the fluid-air interface in the porous layer, $r = R_p$,

$$\int_R^{R_p} \frac{\partial p}{\partial r}\,\mathrm{d}r = \int_R^{R_p} \frac{\mu}{2\pi h_0 k}\frac{dV}{dt}\frac{1}{r}\,\mathrm{d}r. \tag{3}$$

Assuming quasistatic pressure $p_e(t)$ everywhere in the blister, due to deformation of the elastic sheet, then at the boundary of the blister the fluid pressure is $p(r = R, t) = p_e(t)$. Also, we recognize the capillary pressure p_c at the liquid-air interface $R_p(t)$, so that $p(r = R_p, t) = -p_c$, which is the reference atmospheric pressure minus the Laplace pressure jump across the interface. Using Eq. (1), $\frac{R_p(t)}{R} = \sqrt{\frac{V_{tot}-V(t)}{\phi \pi h_0 R^2}}$, Eq. (3) can be written

$$p_e(t) + p_c = -\frac{\mu}{4\pi h_0 k}\frac{dV}{dt}\ln\left(\frac{V_{tot} - V(t)}{\phi\pi h_0 R^2}\right). \tag{4}$$

B. Blister pressure

A fluid-filled blister beneath an elastic sheet has a pressure that is due to the deformation of the elastic sheet. The pressure in the blister is assumed to be quasistatic, meaning we neglect viscous flow within the blister, and the blister shape is assumed to be radially symmetric. We consider two cases: thin sheets ($d/R < 0.1, h \sim d$) where the pressure within the blister is due to bending and stretching of the elastic sheet and thick sheets ($h \ll d$) where bending stresses are the dominant contribution to the pressure.

First we consider the most general case, for elastic sheets with $d/R < 0.1$, the Föppl-von Kármán plate equations for a pressurized blister are

$$p_e(r,t) = D\nabla^4 h - \frac{1}{r}\frac{\partial}{\partial r}\left(\frac{\partial T}{\partial r}\frac{\partial h}{\partial r}\right) \tag{5a}$$

$$0 = \nabla^4 T + \frac{Ed}{2}\frac{1}{r}\frac{\partial}{\partial r}\left(\frac{\partial h}{\partial r}\right)^2, \tag{5b}$$

where $h(r,t)$ is the blister height and $T(r,t)$ is the radial tension in the sheet due to stretching. The Airy function T for the stress potential is defined as $\sigma_{rr} = \frac{1}{r}\frac{\partial T}{\partial r}$ and $\sigma_{\theta\theta} = \frac{\partial^2 T}{\partial r^2}$, where σ_{ij} are the components of the stress tensor. Integrating the height profile defines the blister volume

$$V(t) = \int_0^R 2\pi r h(r,t)\ \mathrm{d}r. \tag{6}$$

The boundary conditions at the center of the blister, $r = 0$, are

$$\frac{\partial h}{\partial r} = \frac{\partial^3 h}{\partial r^3} = \frac{\partial T}{\partial r} = \frac{\partial^3 T}{\partial r^3} = 0. \tag{7}$$

The elastic sheet is adhered to the porous substrate, requiring zero displacement and zero tension in the elastic sheet beyond the edge of the blister, so the boundary conditions at the edge of the blister, $r = R$, are

$$h = \frac{\partial h}{\partial r} = T = \sigma_{\theta\theta} - \nu\sigma_{rr} = 0. \tag{8}$$

1. *Thin elastic sheets*

A scaling analysis of Eqs. (5a) and (5b) shows that the relative magnitude of contributions to the pressure by bending, $\mathcal{E}_B \sim \frac{Dh}{R^4}$, and stretching, $\mathcal{E}_S \sim \frac{Th}{R^4} \sim \frac{Edh^3}{R^4}$, results in $\mathcal{E}_B/\mathcal{E}_S \sim d^2/h^2$. Hence, if $d \sim h$, contributions to the elastic pressure by bending and stretching are comparable in magnitude, as is the case for our experiments using thin sheets, so both terms in Eq. (5a) contribute to the blister pressure.

Using Eq. (4), the set of partial differential equations (PDEs) for blister drainage are Eq. (5b) and

$$D\nabla^4 h - \frac{1}{r}\frac{\partial}{\partial r}\left(\frac{\partial T}{\partial r}\frac{\partial h}{\partial r}\right) + \frac{\mu}{4\pi k h_0}\frac{dV}{dt}\ln\left(\frac{V_{tot} - V(t)}{\phi\pi h_0 R^2}\right) + \gamma\left(\kappa_1 + \kappa_2\right) = 0, \tag{9}$$

which can be solved with Eq. (6), and boundary conditions given by equations (7-8). The first and second terms of Eq. (9) are the contributions to the blister pressure from bending and stretching, respectively. The third term defines the viscous resistance in the porous substrate. The last term is the capillary pressure at the liquid-air interface, where κ_1 and κ_2 are the out-of-plane and in-plane curvatures of the interface, respectively (see Section II C for details).

Dimensionless versions of the variables V, t, r, T, and h are defined by

$$\mathcal{V} \equiv \frac{V}{V_0}, \quad \tau \equiv t\frac{4\pi k h_0 \gamma\left(\kappa_1+\kappa_2\right)}{\mu V_0}, \quad \tilde{r} \equiv \frac{r}{R}, \quad \tilde{T} \equiv \frac{T}{(192)^2 E d V_0^2/\pi^2 R^4}, \quad \tilde{h} \equiv \frac{h}{192 V_0/\pi R^2}, \tag{10}$$

where the timescale is chosen to balance the viscous and capillary terms, since for thin sheets, the capillary pressure is the dominant driving pressure. The dimensionless equations are

$$\frac{1}{\tilde{p}_c}\left(\tilde{\nabla}^4\tilde{h} - \Lambda\frac{1}{\tilde{r}}\frac{\partial}{\partial\tilde{r}}\left(\frac{\partial\tilde{T}}{\partial\tilde{r}}\frac{\partial\tilde{h}}{\partial\tilde{r}}\right)\right) + \frac{d\mathcal{V}}{d\tau}\ln\left(\frac{B-\mathcal{V}}{C}\right) + 1 \;=\; 0 \tag{11a}$$

$$\tilde{\nabla}^4\tilde{T} + \frac{1}{2}\frac{1}{\tilde{r}}\frac{\partial}{\partial\tilde{r}}\left(\frac{\partial\tilde{h}}{\partial\tilde{r}}\right)^2 \;=\; 0 \tag{11b}$$

$$384\int_0^1 \tilde{r}\tilde{h}(\tilde{r},\tau)\ \mathrm{d}\tilde{r} \;=\; \mathcal{V}(\tau) \tag{11c}$$

with dimensionless quantities

$$B \equiv \frac{V_{tot}}{V_0}, \quad C \equiv \frac{\phi\pi h_0 R^2}{V_0}, \quad \Lambda \equiv \frac{(192)^2 E d V_0^2}{D\pi^2 R^4}, \quad \tilde{p}_c \equiv \frac{\pi R^6\gamma\left(\kappa_1+\kappa_2\right)}{192 D V_0}. \tag{12}$$

The dimensionless quantity $\tilde{p}_c$ indicates the relative magnitude of the capillary term to the bending term. For less permeable substrates, small k, and thin sheets, so small D, $\tilde{p}_c$ is large indicating that capillary effects are the dominant drainage mechanism, and the dimensionless bending and stretching terms in Eq. (11a) are small. The corresponding initial conditions are

$$\mathcal{V}(\tau=0)=1, \quad \tilde{h}(\tilde{r},\tau=0)=\tilde{h}_0(\tilde{r}), \quad \tilde{T}(\tilde{r},\tau=0)=\tilde{T}_0(\tilde{r}), \tag{13}$$

where $\tilde{h}_0(\tilde{r})$ and $\tilde{T}_0(\tilde{r})$ are determined using Eqs. (11a-11c). Also, dimensionless boundary conditions at $\tilde{r}=0$ are

$$\frac{\partial\tilde{h}}{\partial\tilde{r}} = \frac{\partial^3\tilde{h}}{\partial\tilde{r}^3} = \frac{\partial\tilde{T}}{\partial\tilde{r}} = \frac{\partial^3\tilde{T}}{\partial\tilde{r}^3} = 0, \tag{14}$$

and at $\tilde{r}=1$,

$$\tilde{h} = \frac{\partial\tilde{h}}{\partial\tilde{r}} = \tilde{T} = \frac{\partial^2\tilde{T}}{\partial\tilde{r}^2} - \nu\frac{\partial\tilde{T}}{\partial\tilde{r}} = 0. \tag{15}$$

2. Thick elastic sheets

For elastic sheets where $h(r,t) \ll d$, the dominant contribution to the fluid pressure in the blister is bending. Neglecting the tension in the sheet, the blister pressure (Eq. (5a-5b)) simplifies to

$$p_e(t) = D\nabla^4 h(r,t). \tag{16}$$

For a fluid blister of radius R under an elastic sheet with bending rigidity D, Eq. (16) is applicable for elastic sheets with aspect ratios $d/R < 0.1$, and solved with boundary conditions $h(r=R,t)=0$, $h'(r=0,t)=0$, $h'(r=R,t)=0$, and $h'''(r=R,t)=0$ (primes denote r-derivatives). These steps give the bell-shaped profile, $h(r,t) = \frac{p_e(t)R^4}{64D}\left(1-\frac{r^2}{R^2}\right)^2$.

The parameters of our experiments often have $d/R > 0.1$, for which the Kirchhoff hypothesis no longer applies because the transverse shear deformations cannot be neglected [22]. Accounting for the contributions of the transverse shear deformations in the elastic sheet gives a modified solution for thick plates, and the height profile of the blister is now

$$h(r,t) = \frac{p_e(t)R^4}{64D}\left(\left(1-\frac{r^2}{R^2}\right)^2 + \frac{4}{1-\nu}\frac{d^2}{R^2}\left(1-\frac{r^2}{R^2}\right)\right). \tag{17}$$

Using Eq. (17) in Eq. (6), the fluid pressure in the blister due to bending deformation of a thick elastic sheet is

$$p_e(t) = \frac{192D}{\pi R^6}\left(1 + \frac{6}{1-\nu}\frac{d^2}{R^2}\right)^{-1} V(t). \tag{18}$$

It follows that Eq. (4) can be written as an ODE for the blister volume $V(t)$,

$$\frac{192D}{\pi R^6}\left(1 + \frac{6}{1-\nu}\frac{d^2}{R^2}\right)^{-1} V(t) + \frac{\mu}{4\pi h_0 k}\frac{dV}{dt}\ln\left(\frac{V_{tot} - V(t)}{\phi\pi h_0 R^2}\right) + \gamma\left(\kappa_1 + \kappa_2\right) = 0, \tag{19}$$

with the initial condition $V(t=0) = V_0$. The first term of (19) is the bending pressure, the second term corresponds to the viscous resistance in the pores, and the last term is the capillary pressure at the fluid-air interface in the pores. For this thick plate limit, we define dimensionless volume and time as

$$\mathcal{V} \equiv \frac{V}{V_0} \quad \text{and} \quad \tau \equiv t\frac{768Dkh_0}{\mu R^6}\left(1 + \frac{6}{1-\nu}\frac{d^2}{R^2}\right)^{-1}, \tag{20}$$

where in contrast with the thin sheet model, the timescale is chosen to balance the bending term with the viscous term. In this case, Eq. (19) becomes the dimensionless ODE,

$$\mathcal{V}(\tau) + \frac{d\mathcal{V}}{d\tau}\ln\left(\frac{B - \mathcal{V}}{C}\right) + \tilde{p}_c = 0, \tag{21}$$

with an initial condition $\mathcal{V}(\tau = 0) = 1$. Dimensionless parameters B and C are defined by Eq. (12)) and

$$\tilde{p}_c \equiv \frac{\gamma\left(\kappa_1 + \kappa_2\right)}{P_e}, \tag{22}$$

where P_e is the characteristic elastic pressure of a blister under a thick elastic sheet, $P_e \equiv \frac{192DV_0}{\pi R^6}\left(1 + \frac{6}{1-\nu}\frac{d^2}{R^2}\right)^{-1}$. For large P_e, $\tilde{p}_c$ is small, and the blister pressure due to bending of the elastic sheet is the dominant drainage mechanism.

C. Capillary pressure

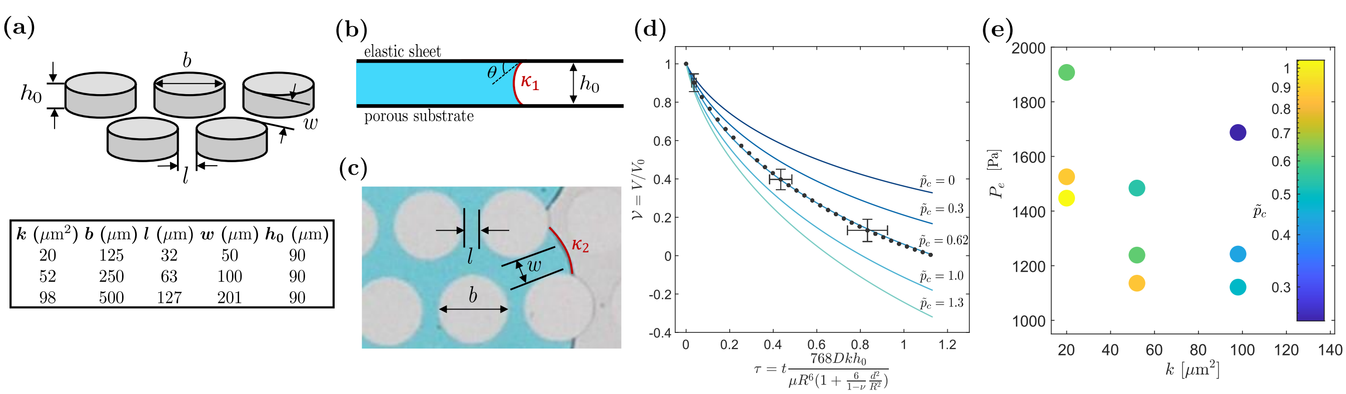

k (μm^2)	b (μm)	l (μm)	w (μm)	h_0 (μm)
20	125	32	50	90
52	250	63	100	90
98	500	127	201	90

FIG. 2. (a) Pillar array geometry for three substrates. (b) Out of plane curvature, κ_1, between the bottom of the porous substrate and the elastic top sheet. (c) In plane curvature, κ_2, between two adjacent pillars. (d) Solutions of Eq. (4) for varying $\tilde{p}_c$ (solid lines) to determine best fit of $\tilde{p}_c$ for an experiment (black dots with representative error bars). (e) Best fit of $\tilde{p}_c$ for experiments of varying characteristic elastic pressure, P_e, and permeability, k.

The liquid draining from the blister displaces air from the porous substrate. The pressure in the liquid at the air-liquid interface in the porous substrate is $p(r = R_p) = -p_c$. The Laplace pressure jump across the interface is $p_c = \gamma(\kappa_1 + \kappa_2)$, where γ is the interfacial tension and κ_1 and κ_2 are the out-of-plane and in-plane curvatures, respectively (see Fig. 2a-c). The out-of-plane curvature is defined as

$$\kappa_1 = \frac{2\cos\theta}{h_0}, \tag{23}$$

where θ is the contact angle (Fig. 2b) and h_0 is the micropillar height. The in-plane curvature κ_2 depends on the pore throat dimensions w and l (Fig. 2a), and a wettability dependent parameter $f(\theta)$,

$$\kappa_2 = \frac{1}{f(\theta)} \frac{2}{(w+l)/2}. \tag{24}$$

The parameter $f(\theta)$ is used to describe the variation of the in-plane curvature as the fluid enters and exits a pore throat, and it ranges in magnitude from 1 for nonwetting substrates to 10 for a highly wetting substrates [23]. We determine the value of $f(\theta)$ for the model by using the average of the best fit of $\tilde{p}_c$ (Eq. (22)) in Eq. (21) and comparing to our experimental data. An example of this fitting is shown in Fig. 2d where $\tilde{p}_c = 0.62$ fits experimental data (see Section III C for details).

III. EXPERIMENTAL METHODS

A. Experimental Setup

The experimental system (Fig. 1a) consists of a porous substrate and an overlying elastic sheet, both made of polydimethylsiloxane (PDMS). The porous substrate is a circular disk, 8 cm in diameter, patterned with micropillars of diameters of 125, 250, or 500 µm (see geometries in Fig. 2a). For all geometries, the porosity, ϕ, of the porous layer is 0.5 and the height of the pillars is $h_0 = 90\,\mu\text{m}$. The permeabilities were measured experimentally to find $k = 20,\ 52,$ and $98\ \mu\text{m}^2$ for arrays with pillar diameters of 125, 250, or 500 µm, respectively. The elastic sheets have an experimentally measured Young's modulus, $E = 1.25 \pm 0.04$ MPa, and varying thicknesses, d. The Poisson ratio of PDMS is $\nu = 0.5$ [24]. The bending modulus of the elastic sheet is given by $D = \frac{Ed^3}{12(1-\nu^2)}$ and we use sheets with bending moduli $D = 5.0 \times 10^{-6} - 3.6 \times 10^{-3}$ Pa m^3, measured experimentally. Both the micropillar arrays and elastic sheets are corona treated before every experiment to increase the wettability of the PDMS. If the PDMS is nonwetting, the blister will only drain either partially or not at all (see Supplemental Material [25]). The was measured to be $\theta = 79 \pm 7^\circ$ after corona treatment, although we note that this is an average and there are variations in the contact angle both spatially over the substrate and in time due to the corona treatment method.

For each experiment, a fluid-filled blister is formed between the substrate and the elastic by injecting glycerol, with viscosity $\mu = 0.8$ Pa s and interfacial tension $\gamma = 64.9$ mN/m, using a syringe pump. The glycerol is dyed blue with Erioglaucine disodium salt at a concentration of 0.38 g/L for visualization. First, fluid invades the pores and, subsequently, as the pressure in the liquid increases, the elastic sheet is peeled and uplifted from the substrate, resulting in a fluid-filled blister. Further injection causes both the fluid front in the pores and the peeling front of the blister to propagate radially. This process is the subject of future work. After injection is stopped, the peeling front of the blister is static and the blister has radius R, and the initial volume of the blister is V_0. The position of the fluid in the pores, R_p, continues to advance radially as the stresses due to the deformation of the uplifted elastic sheet and the capillary pressure at the fluid-air interface in the pores drive drainage of the blister. The blister is illuminated from below using an LED light panel and imaged from the top using a Nikon D5100 camera operating at a frame rate of 0.5 fps until the blister is completely drained. As an example, Fig. 1b shows a time sequence of blister drainage where darker blue indicates larger fluid depth. A similar system was developed and applied to model the relaxation of ice sheet uplift following the drainage of supraglacial lakes on the Greenland Ice Sheet [21].

B. Image Processing

A typical image processing sequence is shown in Fig. 3. The original image is shown with subsequent images cropped to the region of interest. The background image (I_0) is taken before fluid is injected. The captured RGB image with blue dye is first converted to grayscale (I) and subsequently normalized by the background intensity (I/I_0). To remove spatial noise in the image due to the pattern of the pillars, the normalized image is filtered using a Gaussian filter $G(I/I_0)$. The filtered image is segmented into three parts: fluid in the blister, fluid in the pores, and no fluid using two intensity thresholds. The area of these segments, $A_{blister}$ and A_{pores}, representing the area of the blister and of fluid in the pores, respectively, are tracked in time to calculate the blister volume using $V(t) = V_{tot} - \phi h_0 A_{pores}$. Plotting a profile of normalized intensity across the centroid of the blister (Fig. 3b) shows the noise due to the spatial pattern of the pillars. The results in Fig. 3c demonstrate the elimination of the noise after using a Gaussian filter; the results in Fig. 3b-c also satisfy our assumption of constant blister radius R. For $G(I/I_0) = 1$, meaning that the image intensity is equal to the background image intensity, $h = 0$ µm and there is no fluid in the pores. For $G(I/I_0) = 0.9$, there is fluid in the pores but the height of the blister $h = 0$ µm. For $G(I/I_0) < 0.9$, the height of the blister can be measured using a calibration method to correlate $G(I/I_0)$ to a known depth of fluid (see Supplementary Material [25]).

C. Determining $f(\theta)$

To determine the wettability dependent parameter $f(\theta)$, which characterizes the in-plane curvature κ_2 (Eq. 24), we find the best fit of $\tilde{p}_c$ (Eq. (22)) in Eq. (21) for nine experiments with varying permeability and characteristic elastic pressure, $P_e = \frac{192 D V_0}{\pi R^6}\left(1 + \frac{6}{1-\nu}\frac{d^2}{R^2}\right)^{-1}$. Fig. 2d shows an example of the fit, where $\tilde{p}_c = 0.62$ achieves the best fit. Fig. 2e shows the results of the best fits for nine experiments, where for small characteristic elastic pressure and low permeability substrates the best fit of $\tilde{p}_c$ is larger. This result is consistent with the expectation given $\tilde{p}_c$ represents the magnitude of capillary pressure compared to elastic pressure. Using the data in Fig. 2e, we calculate $f(\theta)$ for each of the nine experiments using Eq. 22. Because $f(\theta)$ should be independent of pore geometry and depend only on the contact angle, we use the average value of $f(\theta) = 3.23$ in the model for all pillar geometries. For simplicity, we assume a constant $f(\theta)$ in time. We note, however, that the contact angle is increasing in time (as the effect of the corona treatment decreases), so $f(\theta)$ is likely decreasing over the time of the experiment.

IV. RESULTS AND DISCUSSION

In this section we present experimental results of the blister shape and of the drainage dynamics for blisters beneath both thick and thin elastic sheets. We compare the experimental results with the corresponding theory presented above.

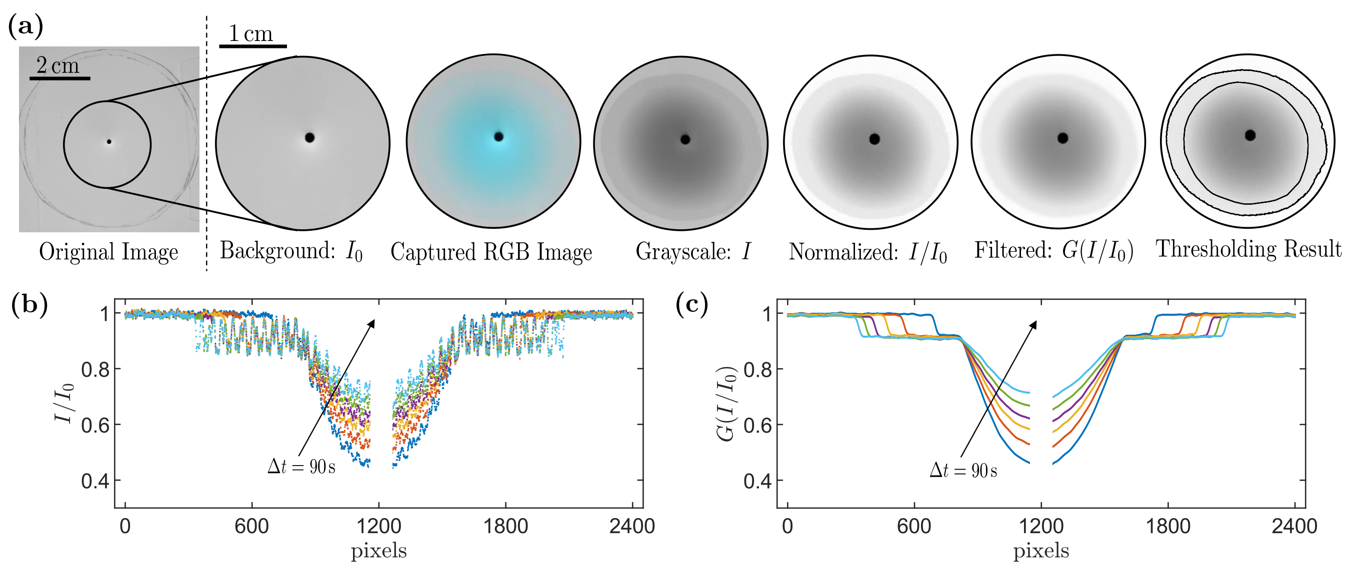

FIG. 3. (a) Image processing to determine the regions of the blister and of the fluid in the pores. (b) Normalized image intensity, I/I_0, profiles through the centroid of the blister are shown for 90 second intervals. Noise is due to the spatial structure of the pillars. Note that at the center, the signal is blocked due to the injection hole. (c) Normalized intensities from (b) are filtered using a Gaussian filter, $G(I/I_0)$, to remove noise. The profiles through the centroid are plotted for 90 second intervals.

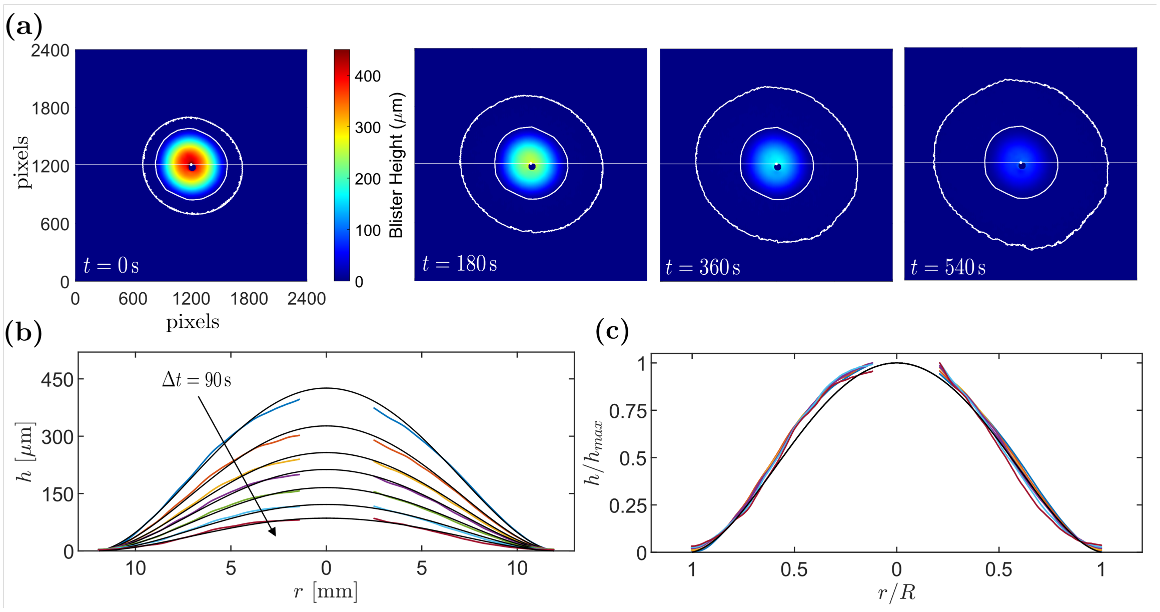

FIG. 4. Blister relaxation experiments. (a) Time sequence of images showing blister height measured using the dye intensity calibration method. The centroid of the blister is shown by the white dot near the injection hole. The subsequent plots are profiles of the horizontal line through the centroid. (b) Blister shape as a function of time. Theoretical blister profiles (black curves, Eqns. 17,18) are plotted using the volume of fluid in the blister calculated from taking the sum of the height of each pixel within the blister at each time step compared to experimental data (colored symbols) (c) Dimensionless blister shape where h is rescaled by the maximum theoretical height, h_{max}, and r is rescaled by R. $R = 11$ mm, $D = 5.7 \times 10^{-4}$ Pa m^3

A. Blister shape

The blister shape is measured using the calibration of dye intensity blister height. After image processing, the filtered images, $G(I/I_0)$ (see Section III B), are converted to height maps using the calibration curves of dye intensity to blister height [25]. A time sequence of the experimentally measured blister shape is shown in Fig. 4a. Small asymmetries in the blister shape are due to non-uniform adhesion between the elastic sheet and the substrate. The non-uniform adhesion also affects the position of the center of the blister with respect to the injection hole, as the blister likely begins to form in a location of low adhesion. Height profiles through the centroid of the blister (horizontal white lines in Fig. 4a) are shown in Fig. 4b as colored symbols for each time point with $\Delta t = 90\,\mathrm{s}$. The experimental height profiles for a blister under a thick elastic sheet show excellent agreement with the theoretical height profiles (black lines), Eqs. (17,18). The total blister volume is calculated by summing the measured height of each pixel within the blister (Fig. 4a). Fig. 4b shows that while the height of the blister is decreasing in time as the fluid in the blister drains into the pores, the blister radius remains approximately constant, which is an assumption of our model. Fig. 4c shows the height rescaled by the maximum height from the theoretical profiles, h_{max}, and the radius rescaled by the blister radius R, which is determined by $R = (A_{blister}/\pi)^{1/2}$. The collapse of the height profiles Fig. 4c shows that the shape of the blister is self-similar in time.

B. Relaxation of blisters under thick elastic sheets

We measure the blister volume as a function of time for substrates with varying permeability k and elastic sheets with varying bending modulus D. The experimental results, shown in Fig. 5a, of six experiments (symbols) exhibit good agreement with the theoretical model Eq. (19) (solid lines). All parameters are measured experimentally, except for $f(\theta) = 3.23$ which was determined by taking the average of the best fit of all experimental data (Section III C). While permeability k and bending modulus D are varied directly, the blister radius R, initial volume V_0, and total volume V_{tot} are varied indirectly and cannot be constrained completely, so we have some variation of these parameters. We observe that the time for relaxation is faster for thicker sheets (large D) and more permeable substrates (large k). Fig. 5b shows the experimental results (symbols) rescaled by a bending-viscous timescale and the dimensionless model Eq. (21) (solid lines).

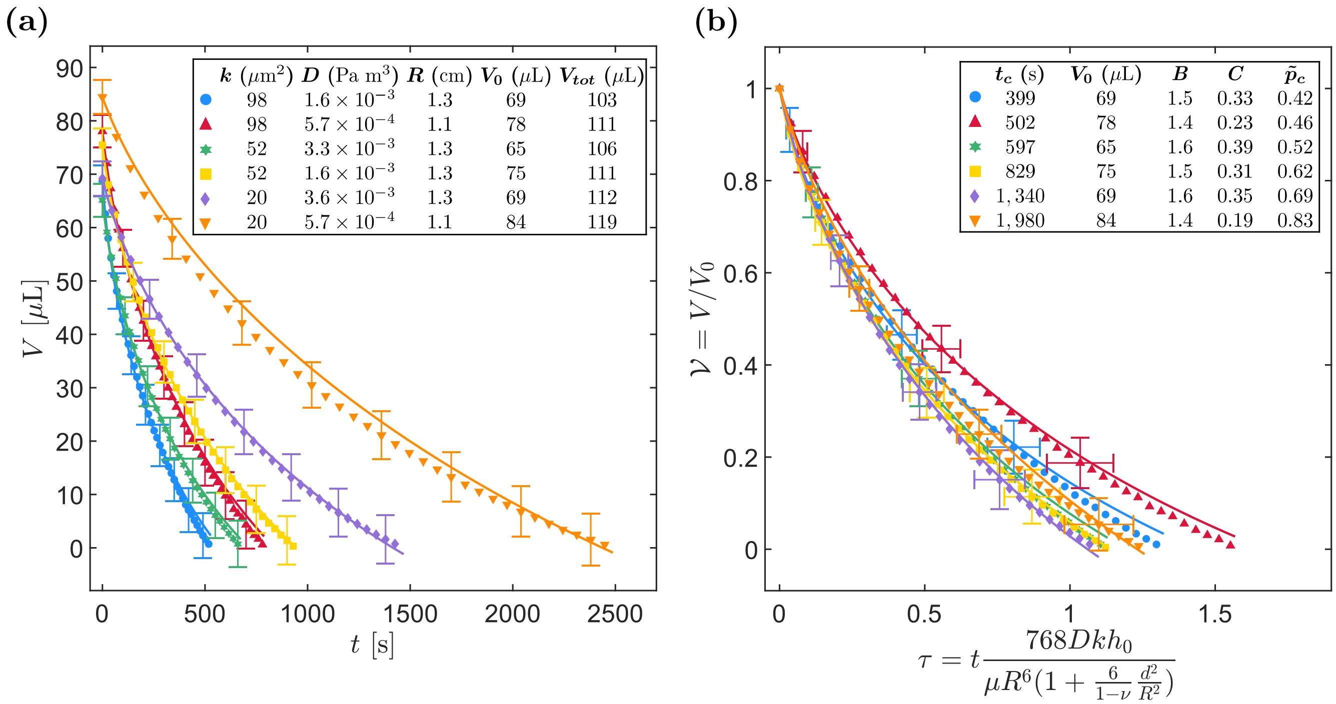

FIG. 5. (a) Blister volume V as a function of time t for varying permeability of the porous substrate, k, bending modulus of the elastic sheet, D, blister radius, R, initial blister volume, V_0, and total volume, V_{tot}. Symbols show experimental results with representative error bars. Solid lines show the solution to the thick elastic sheet model, Eq. (19). (b) Rescaled blister volume $\mathcal{V}$ as a function of rescaled time τ. Solid lines show the solution to the dimensionless thick elastic sheet model, Eq. (21)

There are three dimensionless parameters that account the variations that remain in the dimensionless plot (Fig. 5b). The dimensionless parameters B and C (Eq. 12) represent the ratios of total system volume to initial blister volume and volume of fluid in the pores beneath the blister to the initial blister volume, respectively. B ranges from $1.4-1.6$, so the initial blister volume V_0 is $60-70\%$ of the total volume V_{tot}. Values of C are $0.19-0.39$, so the volume in the pores beneath the blister ranges from $20-40\%$ of the initial blister volume. The dimensionless capillary pressure $\tilde{p}_c$, which is the ratio of capillary pressure to characteristic elastic pressure, is larger for smaller permeability substrates and thinner sheets (meaning smaller bending pressure). The two driving pressures in the system are the dimensionless elastic pressure, $\mathcal{V}$, which is unity at the initial time and zero when the blister is fully drained. The largest dimensionless capillary pressure in our experiments is $\tilde{p}_c = 0.83$, which is comparable to $\mathcal{V}$ at early times, so the drainage due to capillary pressure is important at all times and becomes increasingly dominant at later times when the blister volume decreases. For thicker sheets and more permeable substrates, the capillary pressure has a smaller influence on the relaxation dynamics, e.g., $\tilde{p}_c = 0.42$ in our experiments, meaning that the drainage due to elastic pressure is dominant until $\tau \sim 0.5$ when $\mathcal{V}$ becomes comparable to $\tilde{p}_c$. At later times, the capillary pressure is the dominant drainage mechanism. We note that if the substrate is nonwetting, the blister cannot drain completely because the capillary pressure has the opposite sign and when the elastic pressure is equal to the capillary pressure, drainage will stop, and fluid will remain in the blister (see Supplementary Material [25]).

C. Relaxation of blisters under thin elastic sheets

Experimental results with thin elastic sheets, when there are contributions to the elastic pressure from both bending and stretching (Section II B 1), are shown in Fig. 6. Experimental data are shown by symbols with representative error bars. The dashed lines show solutions to the model (Eq. 5-6) when tension in the sheet is neglected, and solid lines are the solutions to the model with contributions to the elastic pressure from bending and stretching of the sheet. For the thinner sheets (blue circle and red triangle symbols), $D = 5.0 \times 10^{-6}$ and 2.0×10^{-5} Pa m^3, the contribution due to stretching is larger than for the thicker sheet (green star symbol), $D = 1.3 \times 10^{-4}$ Pa m^3. The corresponding dimensionless results are shown in Fig. 6b, where we choose a viscous-capillary timescale. $\tilde{p}_c$ indicates the relative

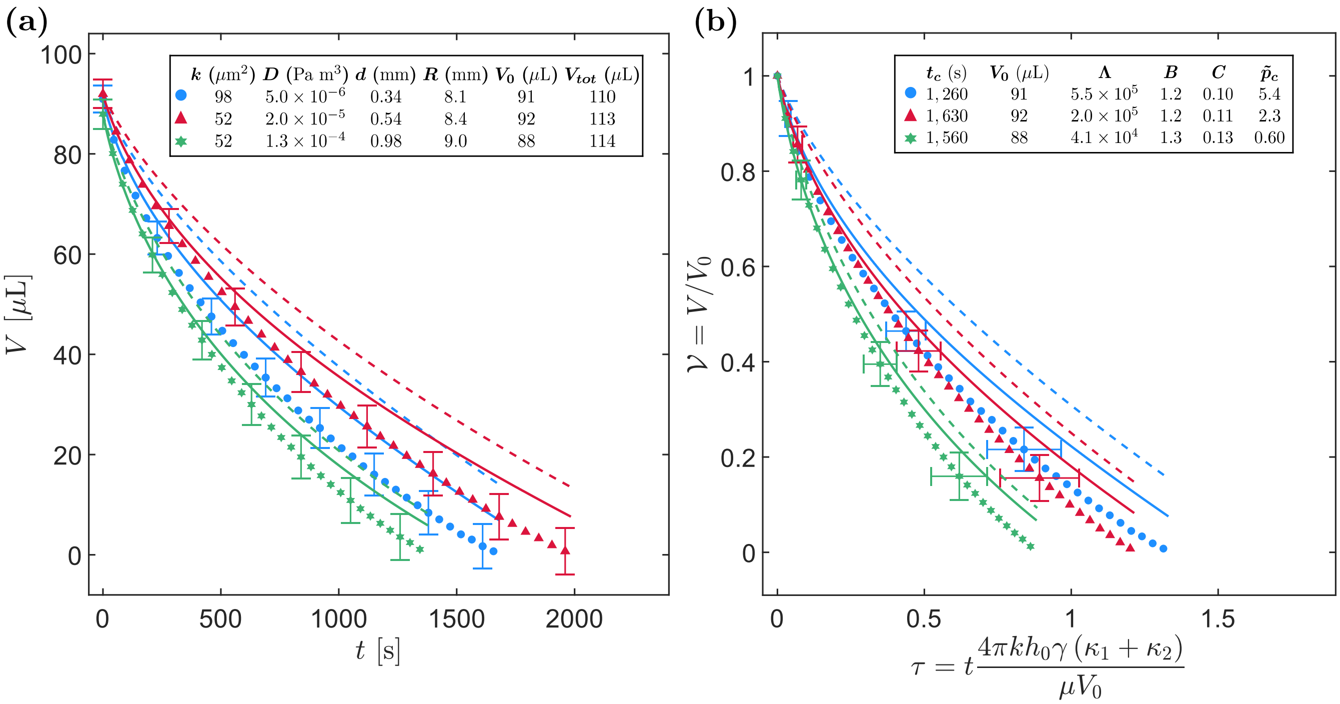

k (μm^2)	D (Pa m^3)	d (mm)	R (mm)	V_0 (μL)	V_{tot} (μL)
98	5.0×10^{-6}	0.34	8.1	91	110
52	2.0×10^{-5}	0.54	8.4	92	113
52	1.3×10^{-4}	0.98	9.0	88	114

t_c (s)	V_0 (μL)	Λ	B	C	$\tilde{p}_c$
1,260	91	5.5×10^5	1.2	0.10	5.4
1,630	92	2.0×10^5	1.2	0.11	2.3
1,560	88	4.1×10^4	1.3	0.13	0.60

FIG. 6. (a) Blister volume V as a function of time t for varying permeability of the porous substrate, k, bending modulus of the elastic sheet, D, blister radius, R, initial blister volume, V_0, and total volume, V_{tot}. Dashed lines show the solution to the model (Eq. 5-6) neglecting tension in the sheet. The solid lines show the solution to the model including contributions from both bending and stretching.(b) Rescaled blister volume $\mathcal{V}$ as a function of rescaled time τ.

importance of capillary pressure to elastic pressure in the drainage. For thinner sheets (blue circles and red triangles), $\tilde{p}_c > 1$ indicating that drainage is dominated by imbibition for all time. Fig. 6b shows collapse of these data when rescaling with the viscous-capillary timescale. We expect one reason why the drainage occurs faster than the model predicts is that the drainage time is long for thin sheet experiments, and since the contact angle increases in time, the average value of $f(\theta)$ that we use in the model is likely larger than the actual value for late times during the experiment. Decreasing $f(\theta)$, corresponding to a less wetting substrate, would improve the agreement between model and experiment. Decreasing $f(\theta)$, corresponding to a less wetting substrate, would improve the agreement between model and experiment. In both limits of thick and thin sheets, the scalings in time we identify approximately collapse all the data for a wide range of parameters.

V. CONCLUDING REMARKS

We developed an experiment and accompanying model to study the relaxation of a fluid-filled blister on a porous substrate. Our experiment consists of a clear PDMS elastic sheet overlying a micropillar array. We inject viscous fluid between these two layers. First, fluid invades the pores and subsequently, the elastic sheet is peeled and uplifted from the substrate resulting in a fluid-filled blister. Further injection causes both the fluid front in the pores and the fracture front of the blister to propagate radially. After injection is stopped, the fracture front of the blister is fixed, and we measured the volume of fluid in the blister as a function of time. We also measured the shape of the blister by calibrating the dye intensity to the blister height and found that the shape of the blister is self-similar in time. This experimental setup also allows for the study of the formation of the blister, which is the subject of future work.

We model the relaxation dynamics including the deformation of the elastic sheet and the capillary pressure at the liquid-air interface as the driving pressures, and the viscous flow in the porous substrate as resistance of the drainage. We find that for thicker sheets and more permeable substrates, the pressure due to the bending of the elastic sheet primarily drives the drainage of the blister, and for thinner sheets and less permeable substrates, drainage is primarily due to the imbibition of the liquid into the pores.

ACKNOWLEDGMENTS

We acknowledge the Princeton Institute for the Science and Technology of Materials (PRISM) for use of the clean room for fabrication of the micropillar arrays and thank Janine Nunes for her help, and we acknowledge the use of the Princeton Imaging and Analysis Center for SEM images of our micropillar arrays and thank Jason Liu for his help. D.L.C. acknowledges support from the National Science Foundation Graduate Research and Fellowship Program and the High Meadows Environmental Institute at Princeton University through the Walbridge Fund.

[1] E. Detournay, Mechanics of hydraulic fractures, Annual Review of Fluid Mechanics **48**, 311 (2016).
[2] S. Nemat-Nasser, H. Abe, and S. Hirakawa, eds., *Hydraulic Fracturing and Geothermal Energy* (Martinus Nijhoff, 1983).
[3] V. C. Tsai and J. R. Rice, A model for turbulent hydraulic fracture and application to crack propagation at glacier beds, Journal of Geophysical Research: Earth Surface (20032012) **115**, 10.1029/2009jf001474 (2010).
[4] A. M. Rubin, Propagation of magma-filled cracks, Annual Review of Earth and Planetary Sciences **23**, 287 (1995).
[5] J. B. Grotberg and O. E. Jensen, Biofluid mechanics in flexible tubes, Annual Review of Fluid Mechanics **36**, 121 (2004).
[6] L. Casares, R. Vincent, D. Zalvidea, N. Campillo, D. Navajas, M. Arroyo, and X. Trepat, Hydraulic fracture during epithelial stretching, Nature Materials **14**, 343 (2015).
[7] M. Thomsen, A. Hernandez-Garcia, J. Mathiesen, M. Poulsen, D. N. Srensen, L. Tarnow, and R. Feidenhans'l, Model study of the pressure build-up during subcutaneous injection, PLoS ONE **9**, e104054 (2014).
[8] L. Salem, B. Gamus, Y. Or, and A. D. Gat, Leveraging viscous peeling to create and activate soft actuators and microfluidic devices, Soft Robotics **7**, 76 (2020).
[9] M. K. Hubbert and D. G. Willis, Mechanics of hydraulic fracturing, AIME Petroleum Transactions **210**, 153 (1957).
[10] A. Takada, Experimental study on propagation of liquidfilled crack in gelatin: Shape and velocity in hydrostatic stress condition, Journal of Geophysical Research: Solid Earth **95**, 8471 (1990).
[11] C.-Y. Lai, Z. Zheng, E. Dressaire, J. S. Wexler, and H. A. Stone, Experimental study on penny-shaped fluid-driven cracks in an elastic matrix, Proceedings of the Royal Society A: Mathematical, Physical and Engineering Sciences **471**, 20150255 (2015).
[12] J. R. Lister, G. G. Peng, and J. A. Neufeld, Viscous control of peeling an elastic sheet by bending and pulling, Physical Review Letters **111**, 154501 (2013).
[13] T. V. Ball and J. A. Neufeld, Static and dynamic fluid-driven fracturing of adhered elastica, Physical Review Fluids **3**, 074101 (2018).
[14] M. Berhanu, A. Guérin, S. Courrech du Pont, F. Raoult, R. Perrier, and C. Michaut, Uplift of an elastic membrane by a viscous flow, Phys. Rev. E **99**, 043102 (2019).
[15] I. J. Hewitt, N. J. Balmforth, and J. R. D. Bruyn, Elastic-plated gravity currents, European Journal of Applied Mathematics **26**, 1 (2015).
[16] J. C. Flitton and J. R. King, Moving-boundary and fixed-domain problems for a sixth-order thin-film equation, European Journal of Applied Mathematics **15**, 713 (2004).
[17] F. Box, J. A. Neufeld, and A. W. Woods, On the dynamics of a thin viscous film spreading between a permeable horizontal plate and an elastic sheet, Journal of Fluid Mechanics **841**, 989 (2018).
[18] D. R. Hewitt, G. P. Chini, and J. A. Neufeld, The influence of a poroelastic till on rapid subglacial flooding and cavity formation, Journal of Fluid Mechanics **855**, 1170 (2018).
[19] D. I. Garagash, E. Detournay, and J. I. Adachi, Multiscale tip asymptotics in hydraulic fracture with leak-off, Journal of Fluid Mechanics **669**, 260 (2011).
[20] C.-Y. Lai, Z. Zheng, E. Dressaire, G. Z. Ramon, H. E. Huppert, and H. A. Stone, Elastic relaxation of fluid-driven cracks and the resulting backflow, Physical Review Letters **117**, 268001 (2016).
[21] C.-Y. Lai, L. A. Stevens, D. L. Chase, T. T. Creyts, M. D. Behn, S. B. Das, and H. A. Stone, Seasonally evolving hydraulic transmissivity beneath greenland supraglacial lakes, Nature Communications (Accepted).
[22] A. C. Ugural, *Stresses in Beams, Plates, and Shells*, 3rd ed. (CRC Press Taylor & Francis Group, Boca Raton, FL, 1981).
[23] B. K. Primkulov, A. A. Pahlavan, X. Fu, B. Zhao, C. W. MacMinn, and R. Juanes, Signatures of fluidfluid displacement in porous media: wettability, patterns and pressures, Journal of Fluid Mechanics **875**, R4 (2019), 1906.02364.
[24] I. D. Johnston, D. K. McCluskey, C. K. L. Tan, and M. C. Tracey, Mechanical characterization of bulk Sylgard 184 for microfluidics and microengineering, Journal of Micromechanics and Microengineering **24**, 035017 (2014).
[25] Supplemental material.